

# Reaction Control System Aerodynamic Interaction Effects on Space Shuttle Orbiter

J. R. Rausch\*

*General Dynamics Convair Division, San Diego, Calif.*

and

B. B. Roberts†

*NASA Lyndon B. Johnson Space Center, Houston, Texas*

This paper presents an analysis of data obtained from wind tunnel tests of the aerodynamic interference induced by the reaction control system jets on Space Shuttle orbiter configurations. The test data was obtained using cold gas simulation techniques with nozzles scaled to match jet exit momentum ratio as the primary parameter at Mach numbers from 2.5 to 10.0. Significant induced effects have been found that degrade the performance of the pitch and roll reaction controls and that induce cross-coupling effects for yaw reaction control. Analysis of the induced data shows good correlation with jet exit momentum ratio.

## Nomenclature

$A$	= area (ft <sup>2</sup> )
$b_{ref}$	= lateral-directional reference length (ft)
$\bar{c}$	= wing chord reference length (ft)
$C_r$	= body axis rolling moment coefficient
$C_m$	= body axis pitching moment coefficient
$C_N$	= body axis normal force coefficient
$C_n$	= body axis yaw moment coefficient
$C_t$	= thrust coefficient = thrust/ $q S_{ref}$
$C_y$	= body axis side force coefficient
$d$	= diameter (ft)
$K$	= force or moment amplification factor
$l$	= location of the jet downstream from leading edge (ft)
$L$	= body length (ft)
$M$	= Mach number
$P$	= pressure (lbf/ft <sup>2</sup> )
$q$	= dynamic pressure (lbf/ft <sup>2</sup> ) R
$R$	= gas constant (ft <sup>2</sup> /sec <sup>2</sup> -R)
$r$	= radius (ft)
$Re$	= Reynolds number
$S_{ref}$	= wing reference area (ft <sup>2</sup> )
$t$	= time (sec)
$T$	= temperature (R)
$V$	= velocity (fps)
$\alpha$	= angle of attack (deg)
$\beta$	= angle of yaw (deg); also $\sqrt{M^2 - 1}$
$\gamma$	= ratio of specific heat
$\phi$	= momentum parameter (lbf) (see Table 2)
$\epsilon$	= nozzle expansion ratio
$\theta_N$	= nozzle exit angle (deg)
<b>Subscripts</b>	
$a$	= ambient conditions
$c$	= rocket chamber condition
$i$	= initial condition
$j$	= jet exit condition
$o$	= total conditions

$t$	= throat
$p$	= peak
$\infty$	= freestream condition
1	= conditions upstream of normal shock
2	= local conditions outside of nozzle exit
Control	= resultant control moment as sum of thrust and induced terms
Thrust	= RCS term
Interaction	= aerodynamic interaction term
Induced	= sum of interaction and impingement terms
Impingement	= plume impingement term

## Introduction

THE Space shuttle orbiter has two reaction control systems (RCS) that perform a number of operations within the Space Shuttle mission profile. Figure 1 shows the location of the forward reaction control engines mounted in the nose section of the orbiter and the aft reaction controls mounted on extensions of the orbital maneuvering system (OMS) pods. The forward RCS engines are primarily used in conjunction with the aft RCS engines for exoatmospheric flight maneuvering commencing with external tank separation. They would also be used in the atmosphere for external tank separation during return to launch site (RTLS) mission abort maneuvers in conjunction with the aft RCS. The aft RCS system also provides the primary control from deorbit through the transition to conventional flight. Figure 2 illustrates the aft RCS mission profile operation from deorbit to conventional flight, showing that these reaction controls are the sole source of control until the aerodynamic forces become appreciable and the aerodynamic surfaces take over the static trimming task. The reaction controls are operated in a blended manner with the aerodynamic controls functioning as rate dampers until full aerodynamic control is achieved. Control in yaw is maintained by the side-firing jets in the aft pods until the transition to lower angles of attack after entry establishes vertical fin and rudder effectiveness. After this transition is completed, all RCS operation is terminated.

Preliminary wind tunnel tests conducted to establish the aft RCS control effectiveness uncovered a potentially serious adverse control effect.<sup>1</sup> The complexity of the flowfield discounted predicting such an effect in that normal jet-flow interactions on the surface having the jet efflux were not the predominant cause. Neither could plume impingement predic-

Presented as Paper 74-1104 at the AIAA/SAE 10th Propulsion Conference, San Diego, California, October 21-23, 1974; submitted October 29, 1974; revision received February 14, 1975.

Index categories: LV/M Dynamics and Control; Entry Vehicle Dynamics and Control; Spacecraft Propulsion Systems Intergration.

\*Design Specialist, Spacecraft Aerodynamics Department.

†Aerospace Engineer. Member AIAA.

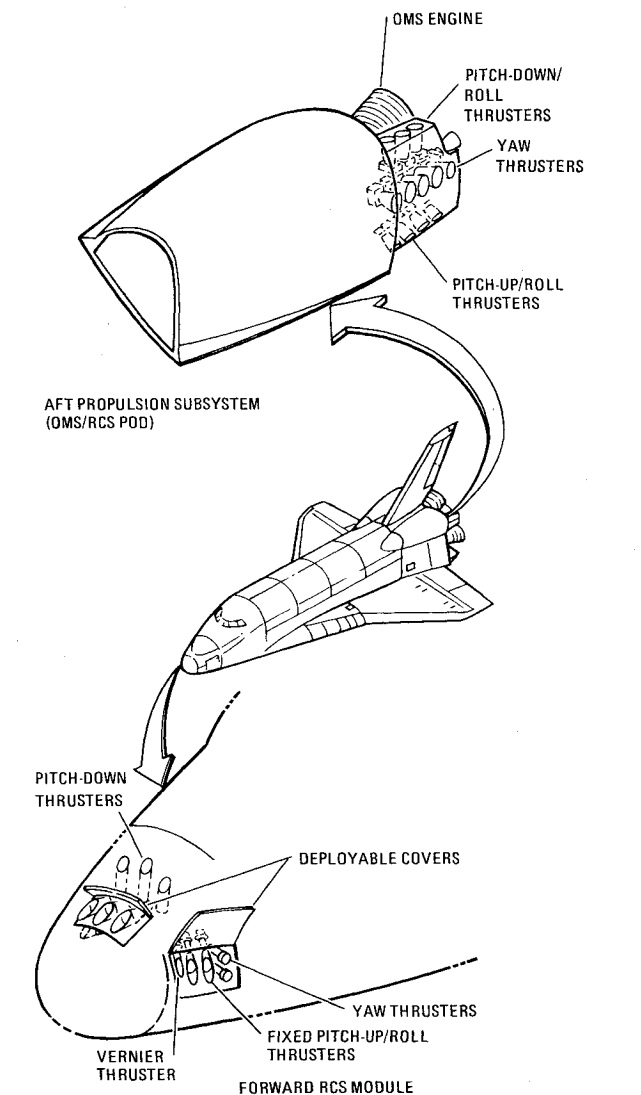


Fig. 1 RCS configuration. 1 fwd RCS module, 2 aft RCS subsystems in pods, 38 main thrusters (14 fwd, 12 per aft pod).

tions yield the usual results, which were a strong function of jet-flowfield interference on adjacent surfaces. The purpose of this paper is to summarize the preliminary test results on the aft RCS showing the unfavorable control effectiveness, illustrate the strong interference effects, and present an empirical method development resulting from the initial test series.

Description of Tests

The aerodynamic data was obtained from a number of wind tunnels, including the NASA Ames Research Center's (ARC) 3.5-foot hypersonic tunnel, the NASA Langley Research Center's (LRC) 31-in. continuous flow hypersonic tunnel, and the NASA LRC 4x4 Unitary Plan wind tunnel at Mach numbers from 2 through 10. The data was obtained on

Table 1 RCS engine characteristics

Parameter	139B RCS Engine	PRR RCS Engine
Thrust	T 900 lb (70K ft)	1,110 lb (vacuum)
Chamber Press.	P <sub>c</sub> 150 psia	157 psia
Chamber Temp	T <sub>c</sub> 5,45 PR	2,500 R
Avg Specific Heat	γ 1.232	1.22
Exapnsion Ratio	ε 20	20
Nozzle Lip Angle	θ <sub>n</sub> 9 deg	9 deg
Exit Area	A <sub>j</sub> 72.382 n. <sup>2</sup>	70.88 in. <sup>2</sup>
Propellant	N <sub>2</sub> O <sub>4</sub> MMH	N <sub>2</sub> H <sub>4</sub> hydrazine

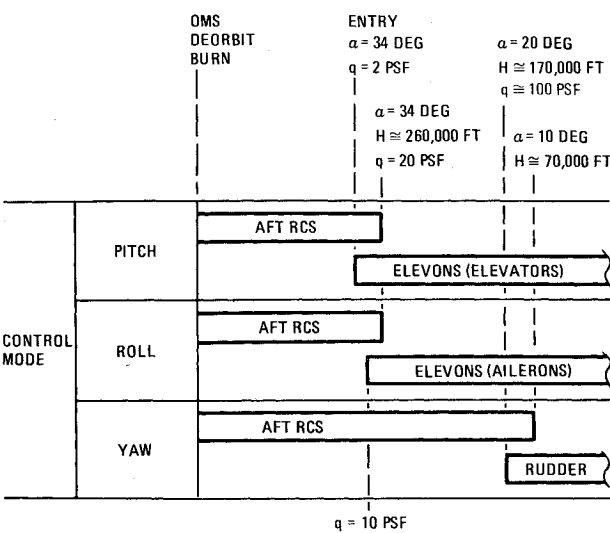


Fig. 2 Aft RCS mission profile.

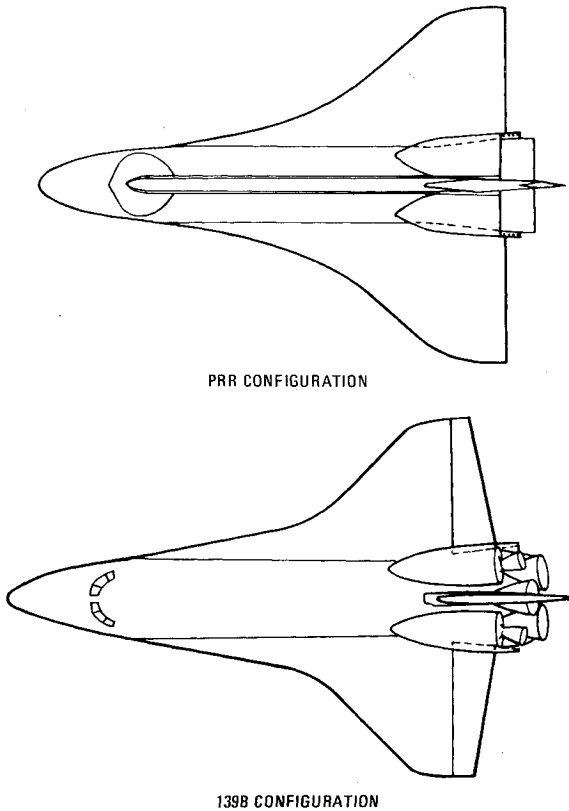


Fig. 3 Configuration sketch.

two orbiter configurations shown in Fig. 3, in which the difference are principally in wing planform and RCS engines. The PRR configuration is an earlier configuration that used hydrazine monopropellant rocket engines for the reaction control system, while the current 139B configuration uses bipropellant nitrogen tetroxide monomethylhydrazine engines. Characteristics of both engines are summarized in Table 1.

Nozzle Scaling

When establishing the simulation requirements for the classic jet interaction flowfield, Spaid and Cassel<sup>2</sup> state the conditions for simulation as: 1) geometric similarity of both body and nozzle; 2) duplication of Mach number ( $M_\infty$ ) and Reynolds number ( $Re_{L_\infty}$ ); and 3) duplication of gas specific

Table 2 Summary of scaling parameters

Jet Characteristics	General Simulation Parameter	Relationship to Momentum Ratio
Boundary in Quiescent Medium	$\left(1 - \frac{P_\infty}{P_j}\right) \frac{\beta_j}{\gamma_j M_j^2}$	$\frac{(P_j - P_\infty) A_j \beta_j}{\phi_j}$
Boundary in Moving Stream	$\left(\frac{P_j - P_2}{P_2 - P_\infty}\right) \frac{P_\infty \beta_j \gamma_\infty M_\infty^2}{P_j \beta_\infty \gamma_j M_j^2}$	$\frac{\phi_j}{\phi_\infty} \left(\frac{P_j - P_2}{P_2 - P_\infty}\right) \frac{\beta_j A_j}{\beta_\infty A_\infty}$
Transmitted Shock	$\frac{P_j \gamma_j M_j^2 \beta_\infty}{P_\infty \gamma_\infty M_\infty^2 \beta_j}$	$\frac{\phi_j}{\phi_\infty} \frac{\beta_\infty A_\infty}{\beta_j A_j}$
Mass Flow	$\left(\frac{P_j^2 \gamma_j M_j^2 (RT)_\infty A_j^2}{P_\infty^2 \gamma_\infty M_\infty^2 (RT)_j A_\infty^2}\right)^{1/2}$	$\frac{\phi_j}{\phi_\infty} \left(\frac{\gamma_\infty R_\infty T_\infty M_\infty^2}{P_j R_j T_j M_j^2 \gamma_j}\right)^{1/2}$
Kinetic Energy	$\frac{\gamma_j M_j^2 (RT)_j}{\gamma_\infty M_\infty^2 (RT)_\infty}$	$\frac{\phi_j}{\phi_\infty} \frac{P_\infty A_\infty R_j T_j}{P_j A_j R_\infty T_\infty}$
Momentum	$\frac{P_j \gamma_j M_j^2 A_j}{P_\infty \gamma_\infty M_\infty^2 A_\infty}$	$\frac{\phi_j}{\phi_\infty}$
Thrust	$\frac{A_j}{A_\infty \gamma_\infty M_\infty^2} \left[ \frac{P_j}{P_\infty} (1 + \gamma_j M_j^2) - 1 \right]$	$\frac{\phi_j}{\phi_\infty} + \frac{A_j (P_j - P_\infty)}{\phi_\infty}$

heat ratio ( $\gamma_j$ ), total temperature ratio ( $R_j T_{oj}/R_\infty T_\infty$ ), and total pressure ratio ( $P_{oj}/P_\infty$ ).

Matching all these parameters may be possible in a limited number of jet interaction controls on missile configurations, but is impossible for the Space Shuttle orbiter RCS during entry since the primary area of concern is at Mach numbers in excess of 20. Thus, one is forced to choose from lists of possible simulation parameters, such as Pindzola's<sup>3</sup> in Table 2, to select those of greatest importance and to design nozzles that simulate the selected parameters. One key idealization of most analyses of plume problems is that the momentum within the plume is conserved, and a jet can be characterized by its momentum flux at the nozzle exit. Taking this as the primary parameter, Table 2 also relates the other parameters to momentum ratio. Jet exit pressure ratio ( $P_j/P_\infty$ ), scaled exit area ratio ( $A_j/A_\infty$ ), gas temperature ratio ( $RT)_j/(RT)_\infty$ , and exit Mach number ratio ( $M_j/M_\infty$ ) comprise the important remaining parameters. The PRR configuration tests concentrated on momentum ratio  $\phi_j/\phi_\infty$ , jet exit pressure ratio  $P_j/P_\infty$ , and scaled nozzle area matching  $A_j/A_\infty$  (which also matches thrust ratio) as the primary matching parameters. The later tests have concentrated on momentum ratio, thrust ratio, and plume boundary at the wing. The primary test simulation used cold gas nitrogen or air as the test gas. The effect of gas temperature ratio,  $(RT)_j/(RT)_\infty$ , was tested very recently using gas mixtures in cold gas simulations.

The small size of the RCS thrust force relative to the aerodynamic forces on the vehicle is illustrated in Fig. 4. The correct simulation of RCS thrust in a wind tunnel would result in a force below the usual quoted wind tunnel balance accuracy ( $1/2\%$  of full scale), but three factors helped in achieving usable results: 1) the most critical region is at lowest dynamic pressures where RCS forces are high relative to aerodynamic forces; 2) the RCS uses a minimum of two engines, increasing RCS forces relative to aerodynamic forces; and 3) the quoted balance accuracy was found to be conservative, approaching a 2-sigma standard deviation value of error in a careful test. Error analyses<sup>4,5</sup> were made for test data on both configurations by performing a number of

Table 3 Balance error summary

Component Coefficient	Error		
	$1/2\%$ of Full Scale	Measured Root Mean Square	Most Probable Error
a. Normal Force (C <sub>N</sub> )	0.0381	0.0107	0.0072
b. Side Force (C <sub>Y</sub> )	0.0095	0.0020	0.0013
c. Pitching Moment (C <sub>m</sub> )	0.00966	0.00277	0.00186
d. Yawing Moment (C <sub>n</sub> )	0.00126	0.000250	0.000167
e. Rolling Moment (C <sub>l</sub> )	0.00126	0.000356	0.000239
Reference Conditions			
Mach	= 4.0		
q	= 145 psf		
S <sub>REF</sub>	= 0.7245 ft <sup>2</sup>		
$\bar{c}$	= 0.6569 ft		
b	= 1.2596 ft		

repeat runs, establishing mean values, and computing actual error deviations for this RCS data. Table 3 presents a summary of the errors of the coefficients showing that the most probable error in the test data is much better than the quoted  $1/2\%$  of full scale. Although, as Fig. 5 shows, the probable balance error is still a significant part of the data, it remains tolerable on control moments for wind tunnel simulations of flight conditions below a dynamic pressure of 35 psf, which fortunately is the region of principal interest.

RCS Jet Exhausting Parallel to the Wing

Figure 1 showed that the yaw jet exhausts from the side of the OMS pod in a plane nearly parallel to the wing. Oil flow visualization with the RCS off showed that the separated flow from the wing reattached to the body at the front of the OMS/RCS pod and a reattachment region swept down the

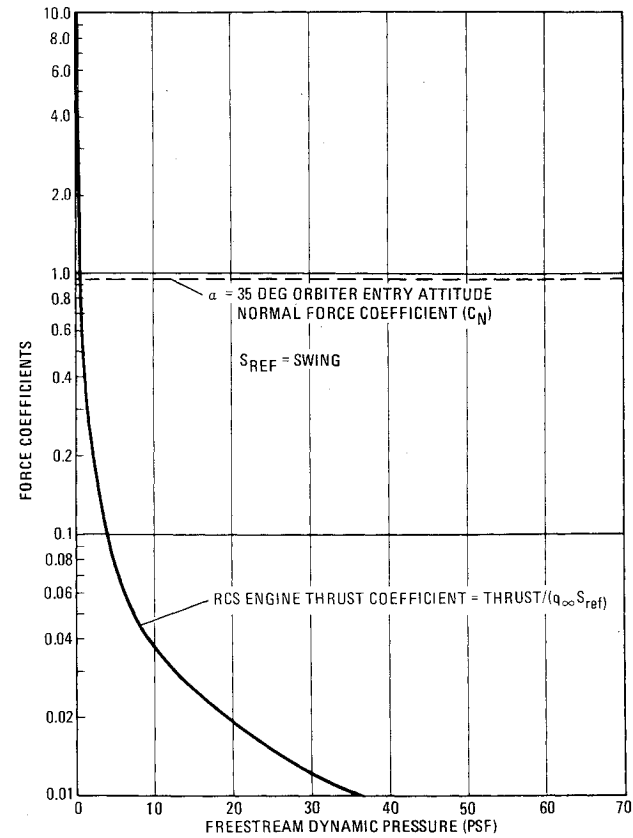


Fig. 4 Relative magnitude of RCS control compared to vehicle aerodynamics.

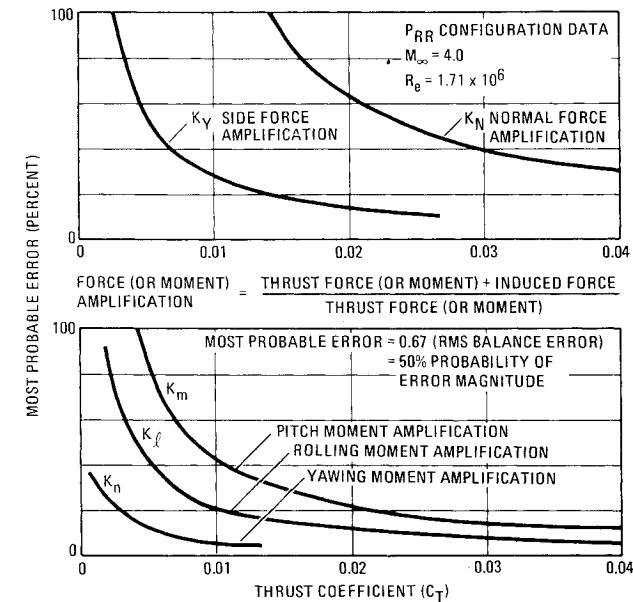


Fig. 5 Most probable error in amplification factor.

side of the pod in a horizontal line in the plane of the yaw thrusters. Turning two RCS jets on resulted in a small region of classic jet interaction on the pod immediately ahead of the jets, which pushed the reattached wing flow upward on the pod. In addition, a large region of plume impingement appeared on the wing trailing edge with its center at about the quarter chord of the wing and with interference flow effects extending along the trailing edge from root to tip caused by the external flow deflecting the yaw plumes down onto the wing.

Figure 6 presents representative test data showing the incremental moment that resulted from the yaw jets blowing

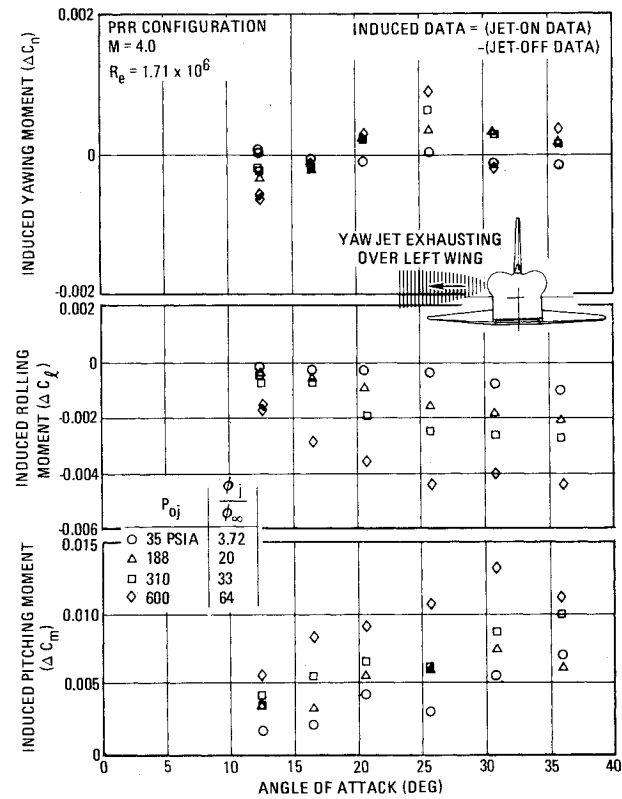


Fig. 6 RCS yaw jet induced moments.

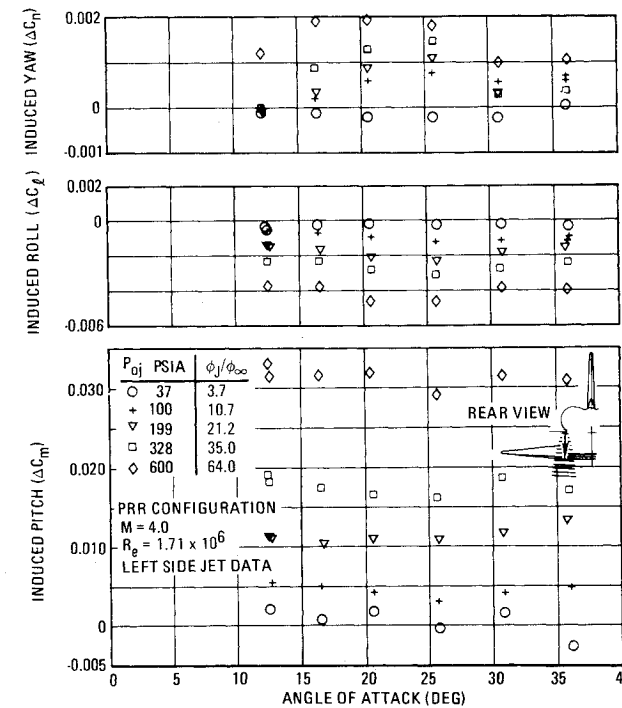


Fig. 7 Induced effects of RCS jet firing toward wing.

over the wing. Very little yawing moment resulted from the jet interaction on the body, but large amounts of nose-up pitching moment and wing-down rolling moment resulted. The induced loads can be seen to be dependent on angle of attack and jet pressure. The small values of the induced yawing moment caused by the yaw jets were within the balance accuracy, and it appears that they are negligible compared to the yawing moment of the jet itself, resulting in a moment amplification factor ( $K_n$ ) equal to 1. The induced roll has a sign opposite that of the yaw RCS thrust moment; the induced

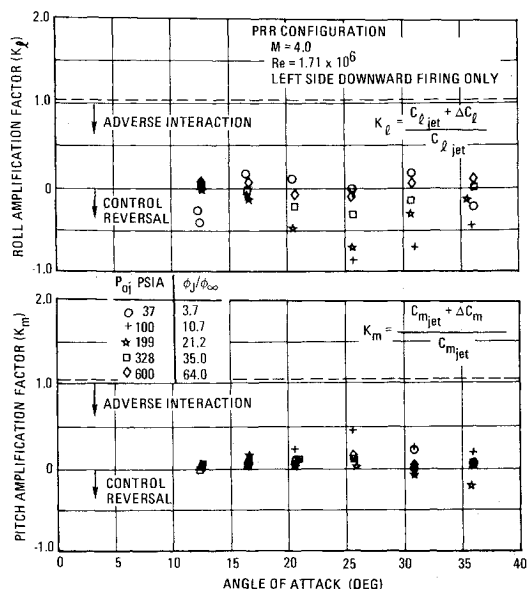


Fig. 8 Moment amplification factors for downward-firing RCS.

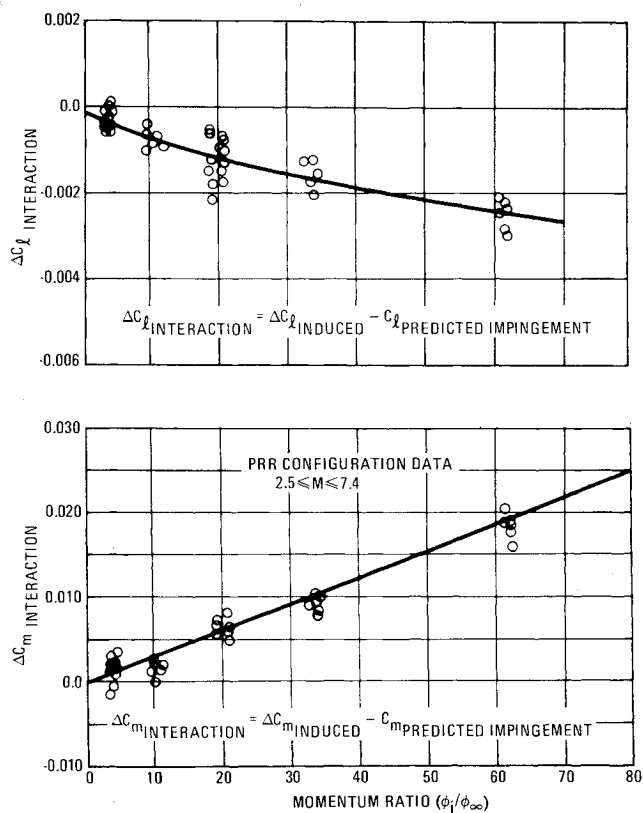


Fig. 9 Downward-firing RCS induced effect correlated with momentum ratio.

pitch is always nose up. Magnitudes of the induced pitch and roll due to yaw RCS are such that from 25% to 50% of the pitch and roll RCS capacity would be required to compensate for these induced moments.

#### RCS Jets Exhausting Toward the Wing

The pitch and roll reaction controls are mounted on the top and bottom of the OMS pod extension and are fired symmetrically for pitch control and differentially for roll control. The downward facing jets fire behind the wing and outboard of the vehicle base and are far from these surfaces (approximately 20 nozzle diameters of a single engine). Oil flow visualization of the RCS exhausting toward the wing showed a

sizeable area of plume impingement emanating from the trailing edge at the wing root. It spread forward on the wing inboard approximately to the leading edge of the OMS pod and to the 50% chord plane outboard on the wing. This plume flow interacts with the wing flow and results in the stagnation line following the shape of the wing leading edge in the interaction region outboard of the impingement flow. A small amount of impingement flow was also seen on the body flap.

The result of this interaction is shown in the incremental moment data of Fig. 7. These increments are jet-on data minus jet-off data with the RCS jet not on the balance. This PRR configuration data shows a strong nose-up pitching moment, a left wing-down rolling moment, and a nose-left yawing moment caused by the left side downward firing jet. The data is strongly dependent on nozzle pressure and less dependent on angle of attack. The values of induced pitchup and roll are larger than and oppose the RCS control moments so that the net result is control reversal on the PRR configuration as seen in Fig. 8.

Computation of the plume impingement induced moments was performed using an analytic model to define characteristics at the plane of the wing and body flap and Newtonian stagnation pressure across the impingement area. This model was found to give good agreement with vacuum chamber impingement data, but only accounted for approximately 40% of the total induced moments measured in these tests. Based on these results, a model was assumed in which the total induced moment was the sum of a direct impingement term and a plume/flow interaction term. The total induced moment data of Fig. 9 was corrected by removing an analytic prediction of plume impingement moment. The residues of the computation were defined as interaction increments, and this data was correlated against the various nozzle flow parameters, such as given in Table 2.

The interaction portion of the incremental moments was found to correlate well with jet exit momentum ratio as shown in Fig. 9, and an empirical model was derived for the jets exhausting toward the wing in which impingement and interaction are considered separately and linearly added.

$$\Delta C_{\ell \text{ induced}} = C_{\ell \text{ impingement}} + \Delta C_{\ell \text{ interaction}} \quad (1a)$$

$$C_{\ell \text{ impingement}} = \text{predicted impingement rolling moment} \quad (1b)$$

$$\Delta C_{\ell \text{ interaction}} = -0.00012805 (\phi_j / \phi_\infty)^{0.71236} \quad (2)$$

$$\Delta C_{m \text{ induced}} = C_{m \text{ impingement}} + \Delta C_{m \text{ interaction}} \quad (3a)$$

$$C_{m \text{ impingement}} = \text{predicted impingement pitching moment} \quad (3b)$$

$$\Delta C_{m \text{ interaction}} = 0.0002637 (\phi_j / \phi_\infty)^{1.03824} \quad (4)$$

where Eqs. (2 and 4) were derived from the curve fits through the data.

The downward-facing jets of the Rockwell configuration 139B were canted outboard and aft to reduce this problem. Figure 10 shows that these fixes have reduced the total induced pitch effect for the downward-firing jet, but increased the induced roll compared to the PRR configuration data.

#### RCS Jet Exhausting Upward Past Fin

The RCS rockets located on the upper surface of the OMS pod extension and approximately 10 nozzle diameters laterally away from the vertical fin are used to produce nose-up moments and to provide roll when fired in combination with downward facing rockets. Oil flow visualization showed that considerable plume impingement occurred over the vertical fin, involving principally the top half of the fin at lower jet pressure ratios and all of the fin at higher pressure ratios. The plume should not be large enough to reach the fin at its maximum size, so it appears that the wing flow which remains

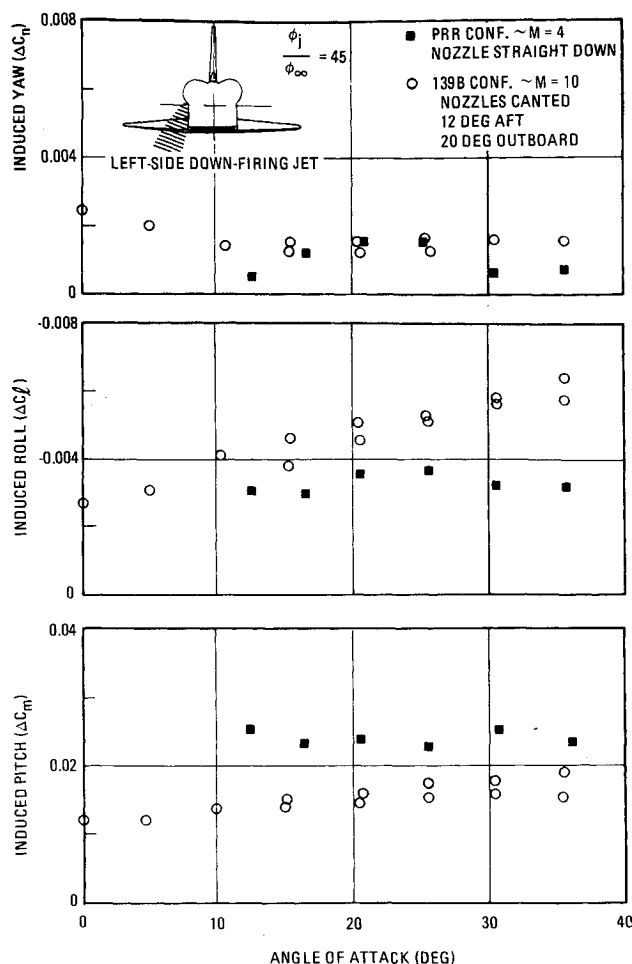


Fig. 10 Effect of configuration differences on induced effects of RCS firing toward wing.

on the OMS pod forces the plume to deflect in the direction of the fin and to impinge upon it.

Figure 11 presents the incremental moments induced on the vehicle by the jet operation and shows that very little pitching moment results because the interaction is primarily on the fin. The incremental rolling moment induced on the fin opposes the roll moment of the upward-firing rocket, and the yawing moment is of the same sign as the RCS roll control. Both the induced yawing moment and rolling moment are strongly dependent on angle of attack and disappear at an angle of about 40°. Figure 12 shows that the peak values of induced moments were correlated with momentum ratio, and the following relations were obtained.

$$\Delta C_{l_{\text{peak}}} = -0.00087037(\phi_j/\phi_\infty)^{0.98545} \quad (5)$$

$$\Delta C_{n_{\text{peak}}} = 0.00011216(\phi_j/\phi_\infty)^{1.0676} \quad (6)$$

Figure 13 shows that the angle of attack at which the peak induced loads occurred also correlates with momentum ratio, and that a limit angle of 39° was found beyond which no induced loads on the fin were encountered. A sine curve relationship was used as an approximation of the incremental effects at angles of attack above and below the angle of peak value. With this approximation, the upward-firing jets are empirically modeled as follows.

at  $\alpha < \alpha_{\text{peak}}$

$$\Delta C_{n_{\text{interaction}}} = \Delta C_{n_{\text{peak}}} \sin \left[ \frac{\alpha \pi}{2\alpha_{\text{peak}}} \right] \quad (7)$$

$$\Delta C_{l_{\text{interaction}}} = \Delta C_{l_{\text{peak}}} \sin \left[ \frac{\alpha \pi}{2\alpha_{\text{peak}}} \right] \quad (8)$$

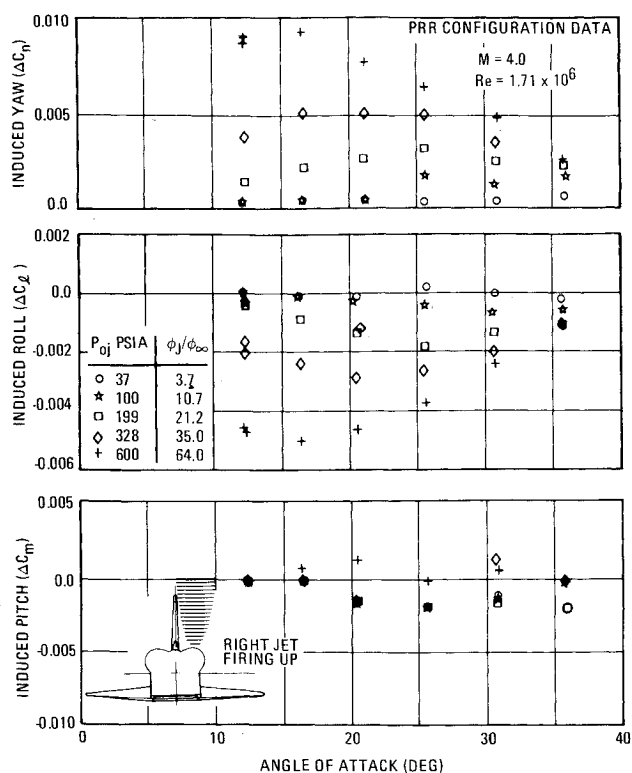


Fig. 11 Induced moments from RCS firing past vertical fin.

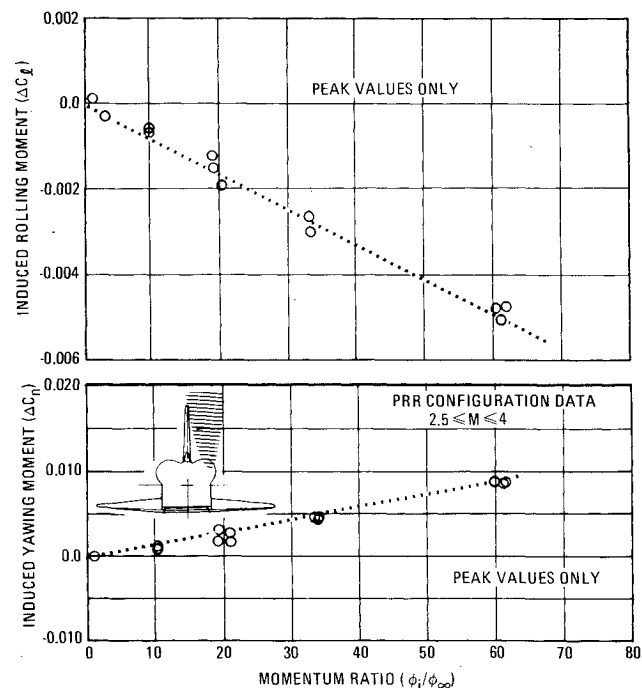


Fig. 12 Peak incremental data for RCS jet interacting with vertical fin.

$$\alpha_{\text{peak}} < \alpha < 39^\circ$$

$$\Delta C_{n_{\text{induced}}} = \Delta C_{n_{\text{peak}}} \sin \left[ \frac{\pi}{2} \left[ \frac{39 - \alpha}{39 - \alpha_{\text{peak}}} \right] \right] \quad (9)$$

$$\Delta C_{l_{\text{induced}}} = \Delta C_{l_{\text{peak}}} \sin \left[ \frac{\pi}{2} \left[ \frac{39 - \alpha}{39 - \alpha_{\text{peak}}} \right] \right] \quad (10)$$

at  $39^\circ < \alpha$

$$\Delta C_{n_{\text{induced}}} = 10 \quad (11)$$

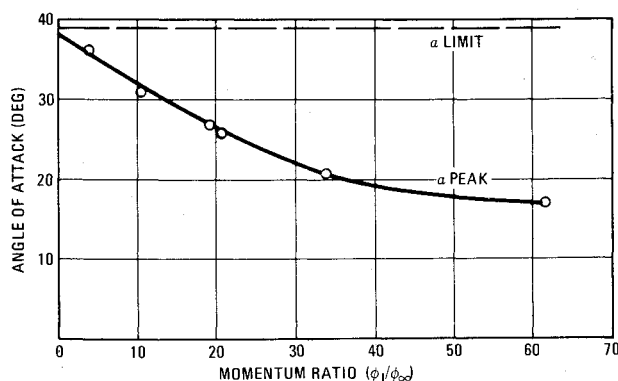


Fig. 13 Peak incremental load correlation.

$$\Delta C_{f_{induced}} = 0 \quad (12)$$

### Other Considerations

Other potential influences are currently under study at this time. The first consideration of future experimental and analytical studies will be the correlation of multiple jets—that is, are the results from multiple jet firings equivalent to the sums of individual jets? This effort will investigate the additivity of one, two, or three or more jets firing in the same axis as well as combinations of jets firing in different axes. As mentioned in the discussion on scaling, Mach number and  $RT$  ratio may also be significant parameters and are under study at this time. One last consideration will be time-dependent effects. Since the minimum impulse for the RCS is 40 msec, there is concern as to whether steady-state testing is a reasonable approximation to the actual prototype case.

### Conclusions

Analysis of the data obtained to date allows the following conclusions to be drawn on induced aerodynamic effects on RCS operation:

1) There are significant induced effects on the Space Shuttle orbiter aerodynamics resulting from reaction control system operation, and it can be expected that any vehicle having jets impinging on a nearby surface will also experience significant effects.

2) These effects are large relative to the control power of the reaction jets and react in a manner to reduce the control effectiveness.

3) The induced effects correlate well with RCS momentum ratio.

4) Additional work is necessary to isolate other correlating parameters so that extrapolations of wind tunnel results to flight condition can be done with high confidence.

### References

- <sup>1</sup>Rausch, J. R. and Roberge, A. M., "RCS Jet-Flow Field Interaction Effects on the Aerodynamics on the Space Shuttle Orbiter," Report CASD-NAS 73-020, Nov. 1973, General Dynamics, San Diego, Calif.
- <sup>2</sup>Spaid, F. W. and Cassel, L. A., "Aerodynamic Interference Induced by Reaction Controls," AGARD-AG-173, Dec. 1973.
- <sup>3</sup>Pindzola, M., "Jet simulation in Ground Test Facilities," AGARDograph 79, Nov. 1963, pp. 13-25.
- <sup>4</sup>Rausch, J. R., "Reaction Control System Aerodynamics Interference Test Report," Report CASD-NAS 73-012, Aug. 1973, General Dynamics, San Diego, Calif.
- <sup>5</sup>Rausch, J. R. and Shih, P. K., "Space Shuttle Orbiter Reaction Control System Jet Interaction Study Interim Report," Report CASD-NSC74-009, Nov. 1974, General Dynamics, San Diego, Calif.

## From the AIAA Progress in Astronautics and Aeronautics Series . . .

### GUIDANCE AND CONTROL—v. 8

Edited by Robert E. Roberson, Consultant, and James S. Farrior, Lockheed Missiles and Space Company.

The twenty-nine papers in this volume on space guidance and attitude control cover ascent, space operations, descent, inertial navigation, inertial components, optical navigation, adaptive systems, and attitude control.

Guidance studies cover launch-time variations, booster injection, station keeping, trajectory analysis and prediction, with various types of perturbation and consequent propellant requirements. Lunar missions are analyzed as a type of four-body problem, and a soft landing terminal guidance system is proposed.

Inertial guidance systems are analyzed and proposed, emphasizing error detection and correction routines as applied to servomechanism theory, recognizing the fundamental limitations of inertial systems. Several inertial system components are analyzed, mainly miniaturized high-precision gyros of several types.

Optical navigation systems considered include infrared, optical Doppler systems, and optical frequency shift detection. Adaptive control systems anticipate future projects and engine-out operational capability. Various satellite attitude control systems are treated, and a number of stabilization systems are considered.

670 pp., 6 x 9, illus. \$16.50 Mem. & List

TO ORDER WRITE: Publications Dept., AIAA, 1290 Avenue of the Americas, New York, N. Y. 10019